PCCP

Accepted Manuscript

ROYAL SOCIETY OF CHEMISTRY

www.rsc.org/pccp

Journal Name

ARTICLE

Investigations on the Vertical Electrical Transport in a-Si:H/nc-Si:H Superlattice Thin Films

Received 00th January 20xx,
Accepted 00th January 20xx

DOI: 10.1039/x0xx00000x

www.rsc.org/

Debajyoti Das* and Debjit Kar

Tuning in the size of silicon nano-crystallites (Si-ncs) has been realized simply by controlling the thickness of nc-Si:H sub-layer (t_{nc}) in the a-Si:H/nc-Si:H superlattice thin films grown by low temperature plasma processing in PE-CVD. The vertical electrical transport phenomena accomplished in superlattice films have been investigated in order to identify its effective utilization in practical device configuration. Reduced size of the Si-ncs at thinner t_{nc} and the associated band gap widening due to quantum confinement effect generates the Coulomb potential barrier at the a-Si/nc-Si interface which in turn obstructs the transport of charge carriers to the allowed energy states in Si-ncs, leading to the Poole-Frenkel tunneling as the prevailing charge transport mechanism in force. The advantages of conduction process governed by Poole-Frenkel mechanism are two-fold. The lower barrier height caused by the a-Si:H sub-layer in the superlattice than the silicon oxide sub-layer in conventional structures enhances the conduction current. Moreover, increasing trapped charges in the a-Si:H sub-layer can arbitrarily increase the current conduction. Accordingly, a-Si:H/nc-Si:H superlattice structures could provide superior electrical transport in stacked layer devices e.g., multi-junction all silicon solar cells.

Introduction

Tune-ability in optical band gap due to quantum size effect of silicon nano-crystals (Si-ncs) has increased the application potential of nano-crystalline silicon (nc-Si) thin films in optoelectronics [1–5] and third-generation photovoltaics.[6–9] In order to accomplish such band gap tuning, superior control over the size of the Si-ncs and subsequent size-distribution can be achieved by various configurations, mostly forming Si-ncs in dielectric matrices and in superlattice structures.[10–13] Among those, nano-scaled superlattice structures with alternate Si-rich layer and Si_3N_4/SiO_2/SiC dielectric layer with high temperature (~1100 °C) post-deposition annealing has attracted substantial attention as they provide spontaneous nano-crystallization and superior size-control.[14–18] However, such an essential high-temperature annealing step makes the process badly device-unfriendly, and the presence of the surrounding dielectric barriers around the Si-ncs severely affects the electrical transport process of the charge carriers. In order to minimize such obstruction in the charge transport, the dielectric layers should be thin enough (~2 nm) and the Si-ncs need to be closely spaced so as to allow the overlapping of the wave-functions in between the adjacent Si-ncs, which are mostly critical in device application.[19] In this regard, low temperature deposition of a-Si:H/nc-Si:H superlattice wherein thin a-Si:H sub-layers provide lower dielectric barrier and the size of the Si-ncs are tuned by the thickness of the ultrathin nc-Si:H sub-layers without post deposition annealing, could significantly improve the device feasibility.

In semiconductor superlattice thin films wherein Si-ncs are surrounded by various barrier layers, diverse electrical conduction phenomena may arise. In superlattice structures consisting of Si-rich layer and SiO_2 barrier layer, space charge limited conduction (SCLC) and the phonon assisted tunneling mechanism may take place.[20,21] In case of silicon nitride barrier layer, Fowler–Nordheim (FN) tunneling and also SCLC have been found to be the dominant conduction mechanism.[22,23] The Poole-Frenkel tunneling (due to the field enhanced thermal excitation of trapped electron into the conduction band) can be the dominant mechanism in various superlattices with different kinds of high dielectric barrier layers.[24] Interestingly, the above said conduction mechanisms available in literature are restricted to the specific superlattice structure in which the crystalline layers are sand-witched between highly dielectric barriers. In addition to that, there are a few reports on the conduction modes dominantly controlled by the size of Si-ncs. The present investigation deals with the electrical transport phenomena prevailing in a-Si:H/nc-Si:H superlattice structures and its dependence on the size of Si-ncs at and around the Bohr radius of Si.

Experimental Details

In forming the superlattice (SL) thin films, the alternative layers of hydrogenated amorphous silicon (a-Si:H) and nanocrystalline silicon (nc-Si:H) wherein Si-ncs are embedded in a-Si:H matrix were

*Nano-Science Group,
Energy Research Unit,
Indian Association for the Cultivation of Science,
Jadavpur, Kolkata – 700 032, INDIA
E-mail (D. Das): erdd@iacs.res.in; Fax: +91(33)24732805

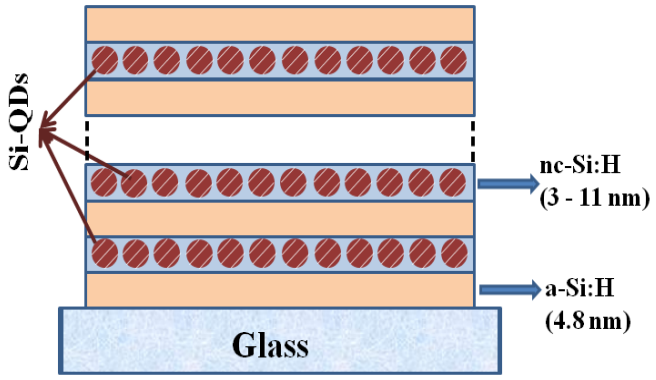

Figure 1. Schematic diagram of the superlattice structure with alternate a-Si:H and nc-Si:H sub-layers.

deposited in a rf (13.56 MHz) capacitively coupled plasma chemical vapor deposition unit from hydrogen diluted silane (SiH_4 + H_2) plasma. During the superlattice formation, the substrate temperature was kept constant at 180 °C and the other deposition parameters were changed for two individual layers. The flow rate of SiH_4 and H_2, gas pressure and the electrical power applied to the plasma were maintained at 95 sccm, 5 sccm, 3 Torr and 15 W for the deposition of a-Si:H layers, while those were changed to 99.5 sccm, 0.5 sccm, 4 Torr and 40 W for growing the nc-Si:H layers. In addition to the effective contribution of specific SiH_n precursors of longer diffusion length from the dissociation of SiH_4 in the plasma, high atomic H density in H_2-diluted SiH_4 at high level of electrical excitation in PECVD has been found to be instrumental in facilitating the growth of nc-Si:H network.[25] Atomic H of the plasma not only acts as the terminator of the dangling bonds but also plays an important role in the chemical reactions during the propagation of the Si network, by offering either topological freedom or chemical potential to the growing surface.[26] Accordingly, for growing the alternate layers of a-Si:H and nc-Si:H, mostly the H_2-dilution and the applied RF power were grossly changed at optimum pressure and fixed substrate temperature. For different SL-thin films, the thickness of the nc-Si:H layers (t_{nc}) were varied between 11 to 3 nm, by changing only the deposition time for each stacking layer, while the thickness of the a-Si:H layers were kept fixed at ~4.8 nm. The deposition rate of the a-Si:H and nc-Si:H sub-layers were estimated from the thickness of the individual bulk layers deposited separately in each case. The SL-thin films were deposited on Corning® Eagle2000™ glass and transparent conducting oxide (TCO) substrates for various structural and electrical measurements. Each SL-thin film was grown with a-Si:H sub-layers on both ends and the total thickness of each sample was maintained at around 200 nm, by changing the number of bi-layers. A schematic diagram for representative superlattice structure has been depicted in Figure 1.

The thickness of the samples was estimated using a Dektak 6M profilometer. Small angle X-ray diffractometry with incident beam at glancing angle (GISAX) was performed with Cu Kα X-ray radiation (λ=1.5418 Å) source in Bruker (D8 Advance) system. The wide angle X-ray diffractometry was done using a Cu Kα X-ray radiation (λ=1.5418 Å) source and a Bragg diffraction set-up (Rich Seifert 3000P). Electrical transport measurement was performed within vacuum of 5×10^{-6} Torr at room temperature in sandwich configuration with circular Al electrodes grown by thermal evaporation on SL-thin films deposited on TCO substrates. The current density was evaluated from the current measured using a Keithley 6517A electrometer.

Results and Discussions

Structural Characterization

Small Angle XRD The periodic structure of the SL-thin films consisting of alternative layers of a-Si:H and nc-Si:H has been investigated from the small-angle XRD (GISAX) in the limited 2Θ-span of 0.5° to 4.0°. For the superlattice thin film with the nc-Si:H layer thickness t_{nc}=11 nm, the 2nd order (m=2) diffraction peak at 2Θ~ 1.16° has been identified, as shown in Figure 2(a), which demonstrates the attainment of periodic structural configuration in the grown material. On gradual decrease in the thickness t_{nc}, the corresponding reduction in the periodic thickness (t_a + t_{nc}) has been endorsed by the systematic shift of the diffraction peaks towards higher magnitude of 2Θ. The 2nd order (m=2) peaks for t_{nc}=11 nm, 8 nm, 6 nm and 4 nm are observed at 2Θ = 1.16°, 1.46°, 1.76° and 1.96°, respectively. The 1st order diffraction peak is expected to appear in such cases at a very low magnitude of 2Θ which is beyond the limit of the present experimental capability. However, the appearance of the 1st order peak with continuously increasing intensity for systematic lowering of t_{nc} is clearly evident from the corresponding curves in Fig. 2(a). In this sequence of reducing the thickness of nc-Si:H sub-layers, for t_{nc}=3 nm the 1st order (m=1) peak has been observed at 2Θ~1.10°. The 1st order peak is so intense that in order to accommodate it within the similar geometric space in a linear scale, the 2nd order peak appears virtually insignificant compared to others (with t_{nc}= 11, 8, 6 & 4 nm). The 2nd order peak is evident in a separate logarithmic plot at the inset of Fig.2(a). The experimental periodic thickness (t_a + t_{nc}) of each SL-thin film has been estimated using Bragg's equation with 1st or 2nd order diffraction peaks and has been compared with the same obtained from conventional measurement of the thickness using surface-profilometer. The excellent linearity of the data points shown by the solid line in Figure 2(b), identifies the consistency of the estimation between samples, while the slope of the plot, Δ= 0.91, demonstrates the excellent one-to-one correspondence in between these two experimental techniques on the evaluation of periodic thickness within the range under investigation.[27–30]

X-ray diffraction studies The variations in the degree of crystallinity in the superlattice films due to reduction in the thickness of nc-Si:H sub-layers (t_{nc}) have been investigated from X-ray diffraction (XRD) studies. The XRD patterns of the SL-films with different t_{nc} have been represented in Figure 3. In case of the bulk (single layer) nc-Si:H film of thickness 200 nm, deposited separately, the corresponding XRD spectrum shows three distinct peaks at 28.4°,

Journal Name

ARTICLE

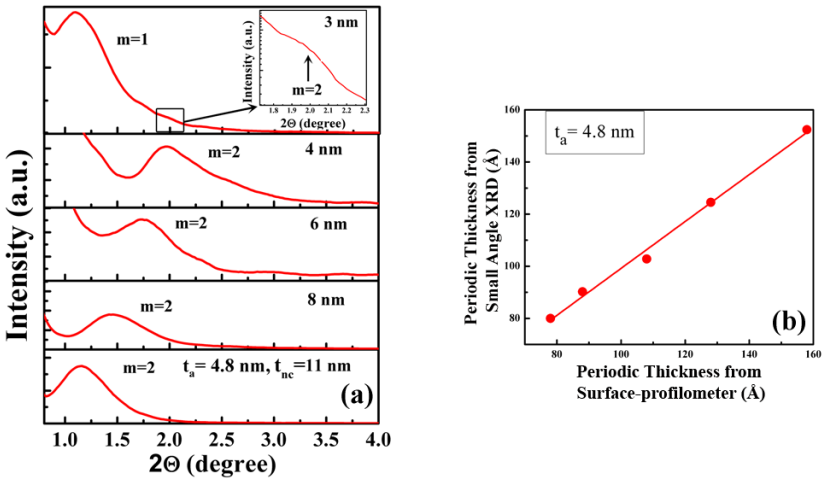

Figure 2. (a) The 1st and 2nd order diffraction peaks obtained in the small angle X-ray diffraction spectra of superlattice films with different thickness (t_{nc}) of nc-Si:H sub-layers. The inset presents the enlarged view of the 2nd order peak for t_{nc}= 3 nm. (b) Periodic thickness (t_a + t_{nc}) of the superlattice films measured from the surface-profilometer showing one-to-one correspondence with the same calculated from the diffraction peak positions.

47.3° and 56.1°, which are identified as <111>, <220> and <311> lattice planes of crystalline silicon, respectively.[10]

For the superlattice structure with t_{nc}=11 nm, the XRD peaks appear at the same positions, however the intensity and the distribution of the peaks have been changed significantly. Each peak continues to reduce in intensity and turns blunt in sharpness on gradual thinning of t_{nc}. For t_{nc} < 6 nm virtually the signature of only the <111> peak is obtained and that persists even for t_{nc} ~3 nm.

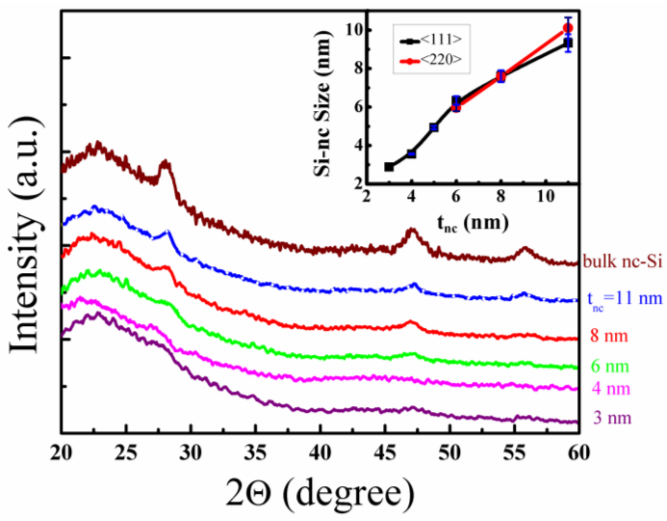

Figure 3. The wide angle XRD of different superlattice thin films showing the diffraction peaks of the crystalline Si. Inset shows the average size of the silicon nano-crystallites as a function of t_{nc}.

Formation of silicon nano-crystals (Si-ncs) even within the ultra-thin (~3 nm) nc-Si:H sub-layer has been made possible owing to the presence of underneath a-Si:H sub-layer that performs as a virtual incubation layer, promoting the formation of Si-ncs at the chosen parametric condition.[25,31] The growth of Si-ncs extends all through the nc-Si:H sub-layers, as evidenced by the almost linear variation of size (d) of Si-ncs (estimated by Scherrer's formula) with the changes in nc-Si:H sub-layer thickness (t_{nc}), shown at the inset of Figure 3.[32]

Transmission Electron Microscopy Studies The physical existence of the Si-ncs in the a-Si:H/nc-Si:H SL-films has been demonstrated by transmission electron microscopy (TEM) studies on representative sample with t_{nc}=6 nm, prepared on carbon coated Cu-grids with 3 bi-layers each of (t_{nc} + t_a) thickness. The plain view TEM micrograph in Figure 4 identifies the deep dark spots as the Si-ncs which are randomly distributed in the relatively bright a-Si matrix. Individual lattice planes of c-Si are clearly identified in the HR-TEM micrograph and the diffraction rings corresponding to <111>, <220> and <311> planes of c-Si are exhibited in the corresponding selected area electron diffraction (SAED) pattern, as shown in the insets. The average size of the Si-ncs appears in the order of nc-Si:H layer thickness (t_{nc}), while the intensity of the diffraction rings of individual planes seems to reduce proportionally as obtained in the X-ray diffraction pattern in Figure 3. Sufficiently high density tiny Si-ncs have been grown even within a narrow thickness of the nc-Si:H sub-layer, t_{nc} ~3 nm, while the size of the Si-ncs has been limited by the thickness of the nc-Si:H sub-layer by terminating its growth in repeated cycles.

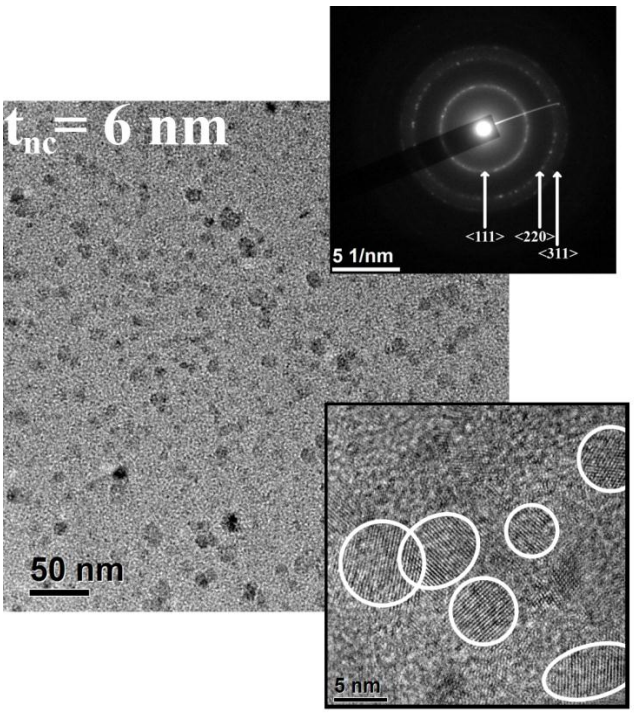

Figure 4. The plain view TEM micrographs of a-Si:H/nc-Si:H superlattice thin films with t_{nc}=6 nm. Insets shows the SAED pattern and high resolution TEM micrograph, demonstrating presence of Si-ncs with different lattice planes.

Electrical Transport Properties

The vertical electrical transport properties of the superlattice thin films have been measured in a sandwich configuration. These films were grown on ITO-coated glass substrates and on the top of the samples Al electrodes were deposited. In order to minimize the difference that may arise between samples, each superlattice film has been grown with identical a-Si:H layer both at the bottom and the top. In spite of this utmost care, uniqueness in the current-voltage characteristics cannot be established because of two different contacts, ITO and Al, at two ends; and that is unavoidable in present experimental configuration. However, it is to be noted that when the electric field was reversed an excellent mirror symmetry was evident in the *J –E* characteristic in each case. In addition, the total thickness of the SL-thin films was maintained at ~200 nm to avoid the thickness dependence of the electrical properties, if any.

Figure 5 shows the variation of the current density (*J*) plotted as a function of applied electric field for different SL-thin films with reducing nc-Si:H layer thickness (t_{nc}) varying from 8 to 3 nm. It has been identified that in each case the current density increased very fast at lower electric fields and gradually attained a virtual saturation. It is noted that the sharpest change in slop of the curves, i.e., the transition point corresponding towards attaining saturation (marked by the arrow in Figure 5), gradually shifted towards higher electric fields on decreasing t_{nc}. Moreover, the saturation current density (J_{Sat}) is of highest magnitude at t_{nc}=8 nm and that reduced very fast for $8 \geq t_{nc} \geq 5$ below which the J_{Sat} attained a virtual overload.

Investigation on the current-voltage characteristics seems to provide adequate methods for distinguishing between the different mechanisms of charge transport for DC conductivity at low and high electric fields. The main mechanisms proposed for the observed behavior include direct tunneling (DT), Schottky emission (SE), Fowler-Nordheim (FN) tunneling, Poole-Frenkel (P-F) conduction and the space charge limited current (SCLC) conduction, depending upon the magnitude of thickness of the barrier layer and its nature of conduction.[33–35] Among those Schottky emission effectively takes place in case of metal-semiconductor junction; again space charge limited current involves the conduction in a doped material, both of which are beyond the present concern. On the other hand, current conduction by direct tunneling occurs across an ultrathin barrier layer.[33] It has been previously reported that for an oxide barrier layer with thickness ~ 5-50 nm, the current conduction is explained by Fowler-Nordheim tunneling.[34]

In a hybrid network in which Si-ncs are embedded in the a-Si:H, a-SiO_x , a-SiN_x or a-SiC_x matrix the prevailing electrical transport phenomena has been discussed in our previous reports.[10,11,36,37] A variety of different electrical conduction phenomena viz., space charge limited conduction (SCLC), Fowler–Nordheim (FN) tunneling, Poole-Frenkel (PF) tunneling, etc have been identified in superlattice structures in which the crystalline layers are sand-witched between highly dielectric barriers e.g., silicon oxide or silicon nitride.[20-24] In order to find the specific electric transport characteristics ensuing in the present set of semiconducting thin films with a-Si:H/nc-Si:H superlattice structure, in particular, the *J*(*E*) data have been fitted to the Poole-Frenkel equation:

$$J = C_1 * E * \exp\left(\frac{-q\left(\phi_B - \sqrt{qE/\pi\varepsilon}\right)}{k_B T}\right) \qquad \text{(i)}$$

$$\text{or, } \ln\left(J/E\right) = \left(\ln C_1 - \frac{q\phi_B}{k_B T}\right) + \frac{q^{3/2}}{k_B T(\pi\varepsilon)^{1/2}} E^{1/2} \qquad \text{(ii)}$$

where, *J* is the current density, *E* is the electric field, C_1 is the proportionality constant, *q* is the charge of carrier (e^- in this case), ϕ_B is the Coulomb barrier height, ε is the dynamic dielectric constant, k_B is the Boltzmann constant and *T* is the temperature.[24,38,39] The SL-thin films with t_{nc} between 8 nm and 3 nm

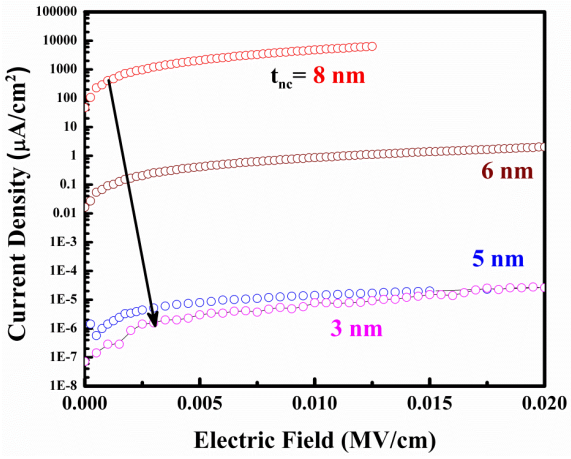

Figure 5. The current density vs. electric field plots for various superlattice thin films.

Journal Name

ARTICLE

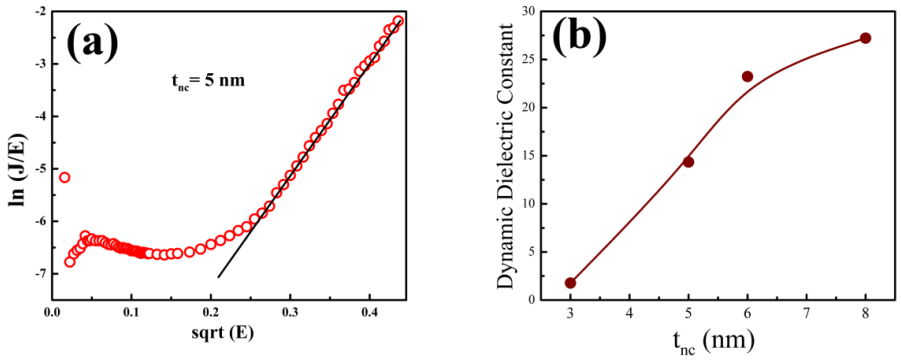

Figure 6. (a) The representative plot of ln(*J/E*) vs. sqrt(*E*) for superlattice thin film with t_{nc}=5 nm showing the validity of Poole-Frenkel mechanism of charge transport. (b) The variation of dynamic dielectric constant with decreasing t_{nc} exhibiting a faster change in magnitude for t_{nc} < 6 nm.

follow the straight line variation in the *ln(J/E)* vs, $E^{1/2}$ plots in individual energy range (as shown in Figure 6(a) for t_{nc}=5 nm), however SL-thin film with t_{nc}=11 nm does not follow the same relation, perhaps due to the larger size of silicon nano-crystallites. It has been noted with interest that the straight line segment in the *ln(J/E)* vs. $E^{1/2}$ plots extends only for a limited range along $E^{1/2}$-axis beyond which *J(E)* enhances very rapidly, rather uncontrollably (data not shown in the plot), which makes it categorically different from the space-charge limited carrier transport[40] where similar straight line plot extends over several decades of magnitude along $E^{1/2}$-axis. Furthermore, the F-N tunneling that occurs due to the tunnel emission of trapped electrons into the conduction band, is followed by the relation: $ln(J/E^2) \propto E^{-1}$ which is not being observed in the present case. Accordingly, it is believed that the Poole-Frenkel (P-F) mechanism of charge transport is in effect for the SL-films under investigation.[20,41]

Poole-Frenkel theory, in general, considers the trapping and de-trapping rates, which modulate the dielectric constant of the films. The dynamic dielectric constant (ε), as measured from the slope of *ln(J/E)* vs. $E^{1/2}$ plots, has been plotted for different t_{nc} in Figure 6(b), showing continuous reduction of ε from 27.22 to 1.77 on gradual decrease in t_{nc}, however, the reduction in the magnitude of ε happens to be significantly fast for t_{nc} <6 nm. In the previous reports by this group it has been shown that in a hybrid network in which Si-ncs are embedded in the a-Si:H or a-SiO_x the optical dielectric constant can be reduced significantly as a consequence of size-reduction of the Si-ncs and/or decaying crystallinity.[42,43] Likewise, in the SL-thin films, the thinning of t_{nc} resulted in the reduced overall crystallinity and also the reduced size of Si-ncs, which might have led to the lowering of the dynamic dielectric constant, making the validity of P-F mechanism more plausible.

Conduction through a dielectric barrier having some trapped charge inside it can be governed by Poole-Frenkel mechanism. In case of present a-Si:H/nc-Si:H superlattice structures, Poole-Frenkel conduction could result from the field-enhanced excitation of charges trapped within the a-Si:H barrier layer into the conduction band of Si-ncs existing within nc-Si:H network. The advantages of conduction process governed by Poole-Frenkel mechanism are two-fold. The barrier height generated by the a-Si:H sub-layer in the superlattice is much lower than the same for the silicon oxide sub-layer in conventional superlattice structures, thereby enhancing the conduction current. Moreover, increasing trapped charges in the a-Si:H sub-layer can arbitrarily increase the current conduction across the superlattice of the ultimate device structure. Accordingly, a-Si:H/nc-Si:H superlattice structures developed in the current work may provide superior electrical transport when used as the active *i*-layer in stacked layer devices e.g., multi-junction all silicon solar cells.

Conclusions

Size of the silicon nano-crystallites (Si-ncs) has been tuned by the thickness of nc-Si:H sub-layer (t_{nc}) in the a-Si:H/nc-Si:H superlattice thin films and the effect of the Si-nc size on the electrical transport properties has been investigated. High density tiny Si-ncs have been grown even within a narrow t_{nc} ~3 nm and it has been made possible by the assistance of the underneath a-Si:H sub-layer, performing as the virtual incubation layer at a specific plasma parameter and thereby promoting the formation of Si-ncs. Formation of the precise super-lattice structures has been acknowledged by the SAX data, while the wide angle XRD results have demonstrated the effectiveness of the nc-Si:H sub-layer thickness (t_{nc}) in controlling the size of Si-ncs. The Poole-Frenkel tunneling has been identified

as the charge transport mechanism, prevailing in the present set of a-Si:H/nc-Si:H superlattice thin films. Reducing size of the Si-ncs at thinner t_{nc} and the associated band gap widening due to quantum confinement generates the Coulomb potential barrier at the a-Si:H/nc-Si:H interface which in turn obstructs the transport of charge carriers to the allowed energy states in Si-ncs, leading to the Poole-Frenkel tunneling mechanism in effect. The advantages of conduction process governed by Poole-Frenkel mechanism are two-fold. The lower barrier height caused by the a-Si:H sub-layer in the superlattice than the silicon oxide sub-layer in conventional structures, enhances the conduction current. Moreover, increasing trapped charges in the a-Si:H sub-layer can arbitrarily increase the current conduction. Accordingly, a-Si:H/nc-Si:H superlattice structures could provide superior electrical transport in stacked layer devices. The a-Si:H/nc-Si:H superlattice films grown by low temperature plasma processing compatible to complementary metal oxide semiconductor (CMOS) technology deserves enormous application potential as active materials in optoelectronics and photovoltaic devices, e.g., multi-junction all silicon solar cells.

Acknowledgements

The work has been done under nano-silicon projects funded by the Department of Science and Technology (Nano-Mission Program) and the Council of Scientific and Industrial Research, Government of India. The HR-TEM studies have been performed using facilities of the Unit on Nano-Science at IACS.

References

1. L. Pavesi, L. Negro, C. Mazzoleni, G. Franzo and F. Priolo, *Nature* 2000, **408**, 440–444.
2. M. Cazzanelli, D. Navarro-Urriós, F. Riboli, N. Daldosso, L. Pavesi, J. Heitmann, L. X. Yi, R. Scholz, M. Zacharias and U. Gösele, *J. Appl. Phys.* 2004, **96**, 3164–3171.
3. D. Das and A. Samanta, *Nanotechnology* 2011, **22**, 055601.
4. N. Daldosso, M. Luppi, S. Ossicini, E. Degoli, R. Magri, G. Dalba, P. Fornasini, R. Grisenti, F. Rocca, L. Pavesi, S. Boninelli, F. Priolo, C. Spinella and F. Iacona, *Phys. Rev. B.* 2003, **68**, 085327.
5. M. Luppi, S. Ossicini, *Phys. Rev. B.* 2005, **71**, 035340.
6. G. Conibeer, M. Green, R. Corkish, Y. Cho, E. C. Cho, C. W. Jiang, T. Fangsuwannarak, E. Pink, Y. Huang, T. Puzzer, T. Trupke, B. Richards, A. Shalav and K. L. Lin, *Thin Solid Films* 2006, **511–512**, 654–662.
7. F. Meillaud, A. Shah, C. Droz, E. Vallat-Sauvain and C. Miazza, *Sol. Energ. Mat. Sol. Cells.* 2006, **90**, 2952–2959.
8. M. A. Green, *Sol. Energ. Mat. Sol. Cells.* 2008, **92**, 1305–1310.
9. B. S. Richards, *Sol. Energ. Mat. Sol. Cells*. 2006, ***90***, 2329–2337.
10. D. Kar and D. Das, *J. Mat. Chem. A* 2013, **1**, 14744–14753.
11. D. Das and B. Sain, *J. Appl. Phys.* 2013, **114**, 073708.
12. M. Dovrat, Y. Goshen, J. Jedrzejewski, I. Balberg and A. Sa'ar, *Phys. Rev. B* 2004, **69**, 155311.
13. C. C. Eun, P. Sangwook, H. Xiaojing, S. Dengyuan, C. Gavin, C. P. Sang and A. G. Martin, *Nanotechnology* 2008, **19**, 245201.
14. N. M. Park, T. S. Kim and S. J. Park, *Appl. Phys. Lett.* 2001, **78**, 2575–2577.
15. J. H. Kim and P. H. Holloway, *J. Appl. Phys.* 2004, **95**, 4787–4790.
16. D. Song, E. C. Cho, G. Conibeer, Y. Huang, C. Flynn and M. A. Green, *J. Appl. Phys.* 2008, **103**, 083544.
17. B. G. Lee, D. Hiller, J. W. Luo, O. E. Semonin, M. C. Beard, M. Zacharias and P. Stradins, *Adv. Funct. Mat.* 2012, **22**, 3223–3232.
18. M. Zacharias, J. Heitmann, R. Scholz, U. Kahler, M. Schmidt and I. Bläsing, *Appl. Phys. Lett.* 2002, **80**, 661.
19. R. B. Dridi, F. Gourbilleau, D. Maestre, O. Palais, A. Sibai, M. Lemiti and G. Brémond, *J. Appl. Phys.* 2012, **112**, 024324.
20. V. Osinniy, S. Lysgaard, V. Kolkovsky, V. Pankratov and A. N. Larsen, *Nanotechnology* 2009, **20**, 195201.
21. Y. K. Kuang, R. H. Pin and L. Po-Tsung, *Nanotechnology* 2013, **24**, 195701.
22. R. Huang, H. Dong, D. Wang, K. Chen, H. Ding, X. Wang, W. Li, J. Xu and Z. Ma, *Appl. Phys. Lett.* 2008, **92**, 181106.
23. J. Warga, R. Li, S. N. Basu and L. Dal Negro, *Appl. Phys. Lett.* 2008, **93,** 151116.
24. J. López-Vidrier, Y. Berencén, S. Hernández, O. Blázquez, S. Gutsch, J. Laube, D. Hiller, P. Löper, M. Schnabel, S. Janz, M. Zacharias and B. Garrido, *J. Appl. Phys.* 2013, **114**, 163701.
25. D. Das, *Solid State Phenom.* 1995, **44**, 227–260.
26. D. Das, *J. Phys. D: Appl. Phys.* 2003, **36** 2335–2346.
27. G. Chen, Y. Guo, Y. Yao, Z. Song and F. Zhang, *Thin Solid Films* 1995, **258**, 132–136.
28. B. Abeles and T. Tiedje, *Phys. Rev. Lett.* 1983, **51**, 2003–2006.
29. G. Han, P. Du, J. Shou and D. Zhao, *Thin Solid Films* 1998, **334**, 6–10.
30. K. Akatsuka, Y. Ebina, M. Muramatsu, T. Sato, H. Hester, D. Kumaresan, R. H. Schmehl, T. Sasaki and M. Haga, *Langmuir* 2007, **23**, 6730–6736.
31. D. Das and M. Jana, *Sol. Energ. Mat. Sol. Cells.* 2004, **81**, 169–181.
32. N. C. Acevedo, J. M. Block and A. G. Marangoni, *Langmuir* 2012, **28**, 16207–17217.
33. J. Maserjian, *J. Vac. Sci. Technol.* 1974, **11**, 996.
34. H. Zhou, F. G. Shi, B. Zhao and J. Yota, *Appl. Phys. A.* 2005, **81**, 767–771.
35. J. F. Scott, *Springer Science & Business Media*. 2000.
36. D. Das and K. Bhattacharya, *J. Appl. Phys.* 2006, **100**, 103701.
37. D. Das and A. Samanta, *Mater. Res. Bull.* 2012, **47**, 3625–3629.
38. S. M. Sze, *J. Appl. Phys.* 1967, **38**, 2951–2956.
39. I. M. Ikram, M. K. Rabinal, M. N. Kalasad and B. G. Mulimani, *Langmuir* 2009, **25**, 3305–3309.
40. F. Chen, B. Li, R. A. Dufresne and R. Jammy, *J. Appl. Phys.* 2001, **90**, 1898–1902.
41. S. Yerci, R. Li and L. Dal Negro, *Appl. Phys. Lett.* 2010, **97**, 081109.
42. A. Samanta and D. Das, *Appl. Surf. Sci.* 2012, **259**, 477–485.
43. D. Das, *Solid State Commun.* 1998, **108**, 983–987.